ADVANCED MATERIALS
www.advmat.de

4.6 V Moisture-Tolerant Electrolytes for Lithium-Ion Batteries

Nan Zhang, Ai-Min Li, Weiran Zhang, Zeyi Wang, Yijie Liu, Xiyue Zhang, Guorui Cai, Hongli Wan, Jijian Xu, and Chunsheng Wang**

Commercial $LiPF_6$-based electrolytes face limitations in oxidation stability (4.2 V) and water tolerance (10 ppm). While replacing $LiPF_6$ with lithium bis(trifluoromethane)sulfonimide (LiTFSI) improves water tolerance, it induces Al current collector corrosion above 3.7 V vs. Li/Li^+. To address this, lithium cyano(trifluoromethanesulfonyl)imide (LiCTFSI) is proposed here as a non-corrosive, moisture-tolerant alternative. The 2.0 M LiCTFSI/propylene carbonate (PC)-fluoroethylene carbonate (FEC) (7:3 by volume) electrolyte enables $LiNi_{0.8}Co_{0.1}Mn_{0.1}O_2$ (NCM811) cathodes to reach 210 mAh g^{-1} (2.8-4.6 V) with a cycle life of 500. Full cells with NCM811||graphite (2.0 mAh cm^{-2}) show 77.8% capacity retention after 500 cycles. Even with 2000 ppm moisture in the electrolyte, full cells maintain high cycling stability, reducing the need for costly dry rooms. The electrolyte's low freezing point and high thermal stability enable the operation from -20 °C to 60 °C, delivering 168 mAh g^{-1} at -20 °C and retaining 94% capacity after 100 cycles at 60 °C. In contrast, cells with commercial $LiPF_6$ electrolyte deliver 71 mAh g^{-1} at -20°C and retain 52.7% after 100 cycles at 60 °C. This novel salt offers a cost-effective solution for developing robust, high-performance batteries suitable for extreme conditions.

1. Introduction

Since their initial commercialization by Sony in 1991, Li-ion batteries (LIBs) have emerged as the preferred power supply for portable electronics. Over the past three decades, significant advancements in energy density have been achieved, surpassing threefold or more compared to their initial commercialization.[1–3] In recent years, LIBs have garnered considerable attention as a promising power solution for electric vehicles (EVs) and stationary energy storage systems, thus playing a crucial role in promoting greener and more sustainable societies.

Despite these advancements, the energy density of ≈270 Wh kg^{-1} for the state-of-the-art commercial Li-ion batteries still falls short of meeting the demanding requirements for emerging applications, particularly EVs, which necessitate a driving range comparable to that of petrol-fueled vehicles. High-nickel layered oxides, such as $LiNi_xCo_yMn_{(1-x-y)}O_2$ (NCM) and $LiNi_xCo_yAl_{(1-x-y)}O_2$, where x is at least 0.8 are considered the competitive choices for cathode materials in EVs due to their high specific capacity (over 200 mAh g^{-1}) and high operating voltage (>4.3 V), which can mitigate range anxiety of EVs.[4,5] However, the commercial electrolytes employing lithium hexafluorophosphate ($LiPF_6$) as salt cannot support high-voltage NCM cathodes. $LiPF_6$ has been utilized as the primary salt in Li-ion batteries for over a decade due to its distinctive combination of properties, including excellent ionic conductivity and the capability to passivate the aluminum current collector. However, $LiPF_6$ electrolytes also suffer high moisture sensitivity to form HF and thermal decomposition at 60 °C.[6–8] HF can induce the dissolution of transition-metal cations, which can migrate to the graphite anode, exacerbating the interfacial impedance.[9,10] Additives such as citraconic anhydride[11] and 3,3′-(Ethylenedioxy)dipropiononitrile[12] are effective in improving the high-temperature tolerance and high-voltage stability of $LiPF_6$-based electrolytes. Furthermore, to completely address the issues associated with $LiPF_6$, borate salts such as lithium bis(oxalato)borate and lithium difluoro(oxalato)borate have been used due to their ability to form stable solid cathode electrolyte interphase (CEI) layers on cathodes. However, these salts are extremely sensitive to water, undergo hydrolysis at ambient temperature, and demonstrate insufficient solubility.[13] Fluorinated sulfonimide salts, featuring a highly conjugated anionic center ($–SO_2–N^–SO_2–$), tend to dissociate well in carbonate solvents, offering high ionic conductivities and thermal stability.[14] Among them, lithium bis(trifluoromethane)sulfonimide (LiTFSI), exhibits thermal stability up to 380 °C and resistance toward hydrolysis. However, LiTFSI shows severe corrosion toward Al current collector at a high operating voltage (>3.7 V).[15] Increasing salt concentration can mitigate corrosion. However, high-concentration electrolytes increased the viscosity and cost, posing challenges for widespread adoption in the industry.[16] Decreasing the solubility of aluminum salts by extending the length of the perfluorinated alkyl chains in sulfonimides offers

N. Zhang, A.-M. Li, W. Zhang, Z. Wang, Y. Liu, X. Zhang, G. Cai, H. Wan, J. Xu, C. Wang
Department of Chemical and Biomolecular Engineering
University of Maryland
College Park, MD 20742, USA
E-mail: jijianxu@umd.edu; cswang@umd.edu

The ORCID identification number(s) for the author(s) of this article can be found under https://doi.org/10.1002/adma.202408039

DOI: 10.1002/adma.202408039

a feasible approach to addressing the aggressive aluminum corrosion behaviors associated with LiTFSI-based electrolytes.[17] A typical example is lithium (trifluoromethanesulfonyl)(nonafluorobutanesulfonyl)imide, which can extend Al corrosion potential to ≈4.8 V versus Li/Li$^+$.[18] However, the extended length of the branch chain greatly increases the molecular mass of the salt, necessitating a higher mass ratio of salt in electrolytes at the same concentration of Li$^+$ (e.g., 1 M), which also increases cost and viscosity. Recently, Qiao et al. reported a non-corrosive sulfonimide salt, lithium (difluoromethanesulfonyl)(trifluoromethanesulfonyl)imide (LiDFTFSI), for 4-V-class rechargeable lithium metal batteries.[14] Due to the chemical instability of the generated Al(DFTFSI)$_3$ in carbonate solvents, a stable passivation layer rich in AlF_3 and LiF helps protect Al, thereby preventing its further anodic dissolution. However, the limited stable voltage of Al at 4.2 V still poses a challenge for high-voltage applications, particularly with high-nickel cathodes (> 4.3 V). As a result, developing new salts with strong Al passivation ability, high-voltage stability, high moisture tolerance, and moderate molecular weight is crucial for advancing next-generation, high-energy density lithium-ion batteries, but still remain as an unsolved challenge.

Herein, we report a carbonate electrolyte employing lithium cyano(trifluoromethanesulfonyl)imide (LiCTFSI) that remarkably improves the high-voltage stability with an Al current collector and enhances moisture tolerance for lithium-ion batteries. 2 M LiCTFSI in propylene carbonate (PC) and fluoroethylene carbonate (FEC) (7:3 by volume) show elevated Al stability even at a high voltage of 4.6 V. The Li($Ni_{0.8}Mn_{0.1}Co_{0.1}$)O_2 (NCM811) cathodes with designed electrolyte retain 80.3% capacity after 500 cycles, with an average coulombic efficiency (CE) of 99.89% at a high cut-off voltage of 4.6 V. When paired with a graphite anode, the NCM811||graphite full cells with areal capacity of 2 mAh cm^{-2} showed 77.8% capacity retention over 500 cycles in cut-off potential of 2.8-4.55 V. Furthermore, the NCM811||graphite full cells are capable of operating in a wide temperature range of-20 to 60 °C. Notably, the electrolyte's moisture insensitivity could potentially reduce production facility requirements and battery manufacturing costs. This approach encourages further exploration into innovative electrolytes with distinct physical and chemical traits, offering a promising direction for future high-energy low-cost lithium-ion batteries.

2. Properties of Salts and Electrolytes

LiCTFSI is an alteration of LiTFSI, where a cyano group replaces one side of the (trifluoromethane)sulfonimide in LiTFSI (**Figure 1a**). LiCTFSI retains the thermal stability characteristic of LiTFSI, as evidenced by the high stability up to 330 °C in the Thermogravimetric Analysis (TGA) (Figure S1, Supporting Information). Additionally, the molecular weight (180.0 g mol^{-1}) of LiCTFSI is comparable to $LiPF_6$ (151.9 g mol^{-1}) and to Lithium bis(fluorosulfonyl)imide (LiFSI, 187.1 g mol^{-1}), but is significantly lower than that (287.1 g mol^{-1}) of LiTFSI. A low molecular weight ensures a low salt weight at the same concentration of Li$^+$ ions. We dissolved the same amount (2M) of LiCTFSI, LiTFSI, and $LiPF_6$ salts into PC-FEC solvents (7:3 by volume) forming three electrolytes with compositions of 2 M LiCTFSI/PC-FEC, 2 M LiTFSI/PC-FEC, and 2 M $LiPF_6$/PC-FEC. As shown in Figure S2a (Supporting Information), the ionic conductivity (2.9 mS cm^{-1}) of the LiCTFSI-based electrolyte is just slightly lower than that (6.2 mS cm^{-1}) of $LiPF_6$-based electrolyte, but is comparable to the value (3.8 mS cm^{-1}) of the LiTFSI-based electrolyte. The high ionic conductivity of $LiPF_6$-based electrolyte is attributed to the smaller volume of the PF_6^- ion. However, the strong interaction (arising ≈ 830 cm^{-1}) between CTFSI$^-$ and the solvent, as revealed by the Fourier Transform Infrared Spectroscopy (FTIR) in Figure S3 (Supporting Information), gives the LiCTFSI-based electrolytes a high lithium transference number (tr_{Li}^+) of 0.8,[19] (Figure S2b, Supporting Information), which can compensate for its relatively low ionic conductivity. In addition, the high thermal stability of LiCTFSI salt also ensures the high stability of LiCTFSI-based electrolytes at high temperatures. As shown in Figure S4 (Supporting Information), the LiCTFSI-based electrolyte remains stable after being stored at 60 °C for a month. In sharp contrast, the $LiPF_6$-based electrolyte suffers from severe decomposition as evidenced by the dark brown color after being stored at 60 °C for a month.

3. Passivation to Al Current Collector

The corrosion of Al current collector in the three electrolytes was investigated by measuring the leak currents of Li||Al cells at 4.6 V versus Li/Li$^+$ at room temperature. As shown in Figure 1b, upon applying the voltage to Al current collector at 4.6 V, the current density of Li||Al cells in $LiPF_6$-based electrolytes promptly decreased and reached a low value of <0.1 μA cm^{-2} within ≈10 min, indicating the excellent passivation capability of $LiPF_6$ toward Al. The current density of Li||Al cells in LiCTFSI-based electrolytes also showed a rapid decrease, followed by a slight increase to ≈5 μA cm^{-2}, and then decreased again to the same level to $LiPF_6$-based electrolytes, demonstrating that LiCTFSI-based electrolytes have a similar passivation capability as $LiPF_6$-based electrolytes. Even at a high temperature of 60 °C, LiCTFSI-based electrolytes also show similar passivation capability to Al current collector as $LiPF_6$-based electrolytes (Figure S5, Supporting Information) after initial high passivation current. In contrast, the initial leak current density of Li||Al cells in LiTFSI-based electrolytes is very high (≈20 μA cm^{-2}), and continuously increases to ≈40 μA cm^{-2}, due to the continuous corrosion of Al current collector. A similar trend is also observed in the cyclic voltammetry (CV) curve of Li||Al cells using different electrolytes. As shown in Figure S6a (Supporting Information), anodic current increases at the potential above 3.5 V in LiCTFSI-based electrolytes. However, in the second anodic scan, the oxidation current is significantly reduced, and the anode current began to increase above 4.5 V, which confirms the passivation of LiCTFSI electrolytes on the Al current collector by forming a robust passivation layer on the Al current collector. In contrast, with the LiTFSI-based electrolyte (Figure S6b, Supporting Information), a rapid increase in anodic current is observed at a potential above 3.7 V, and the current is only slightly reduced in the second anodic scan. During the second cycle, the corrosion current remains significantly higher than acceptable levels. This suggests that LiTFSI fails to passivate the Al current collector by intensifying corrosion after the damage to the original oxide layer. After conducting the potentiostatic corrosion test for 10 h, the cells were disassembled, and the lithium electrode was analyzed using energy-dispersive

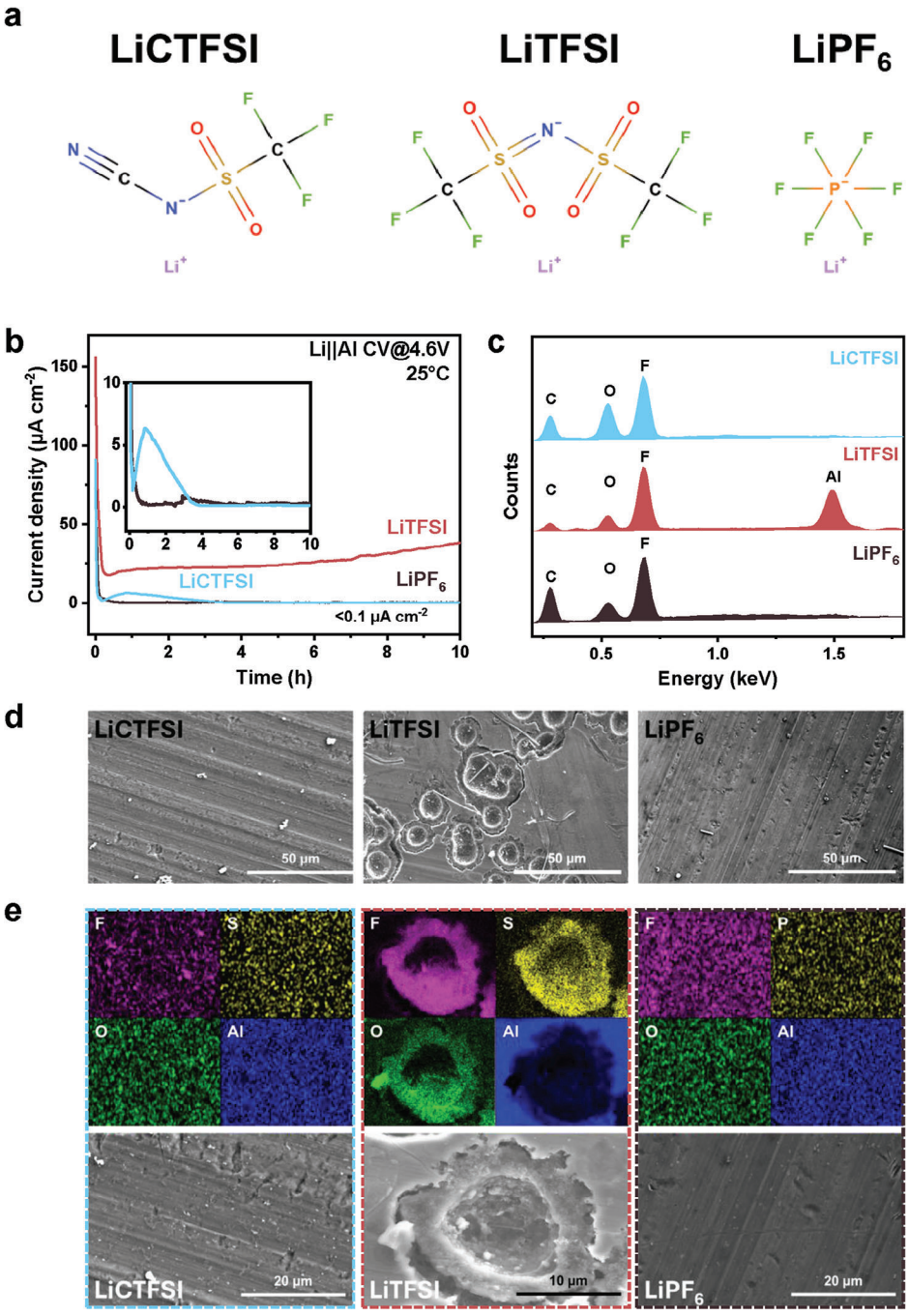

Figure 1. Comparative analysis of Li||Al cells using various electrolytes of PC-FEC (7:3 by volume) with 2 M LiCTFSI, LiTFSI, and $LiPF_6$ at room temperature. a) Molecular structures of LiCTFSI, $LiPF_6$, and LiTFSI salts. b) Leak current density at 4.6 V versus Li/Li^+ at room temperature. The inset image provides a detailed zoom-in for the LiCTFSI and $LiPF_6$ salts. c) EDX results of the Li electrodes after the potentiostatic corrosion test. d) SEM images of the Al current collector after the potentiostatic corrosion test in LiCTFSI-, LiTFSI, and $LiPF_6$-based electrolyte. e) EDX mapping results (top) and the corresponding SEM image (bottom) of the selected area of the Al current collector after the potentiostatic corrosion test. The elements in the EDX mapping are labeled in the top-left corner.

X-ray spectroscopy (EDX). As shown in Figure 1c, besides the C, O, and F peaks derived from the fluorinated salt and carbonate solvents, an obvious Al peak is evident in the spectra obtained. This serves as direct evidence of the dissolution of the Al current collector at elevated voltages in LiTFSI electrolytes, and the dissolved $Al(TFSI)_3$ diffuses toward the surface of Li electrode. In addition, we also conducted a scanning electron microscope (SEM) on the Al current collector after the potentiostatic tests in various electrolytes. As depicted in Figure 1d, the surfaces of the Al current collectors in both LiCTFSI and $LiPF_6$ electrolytes

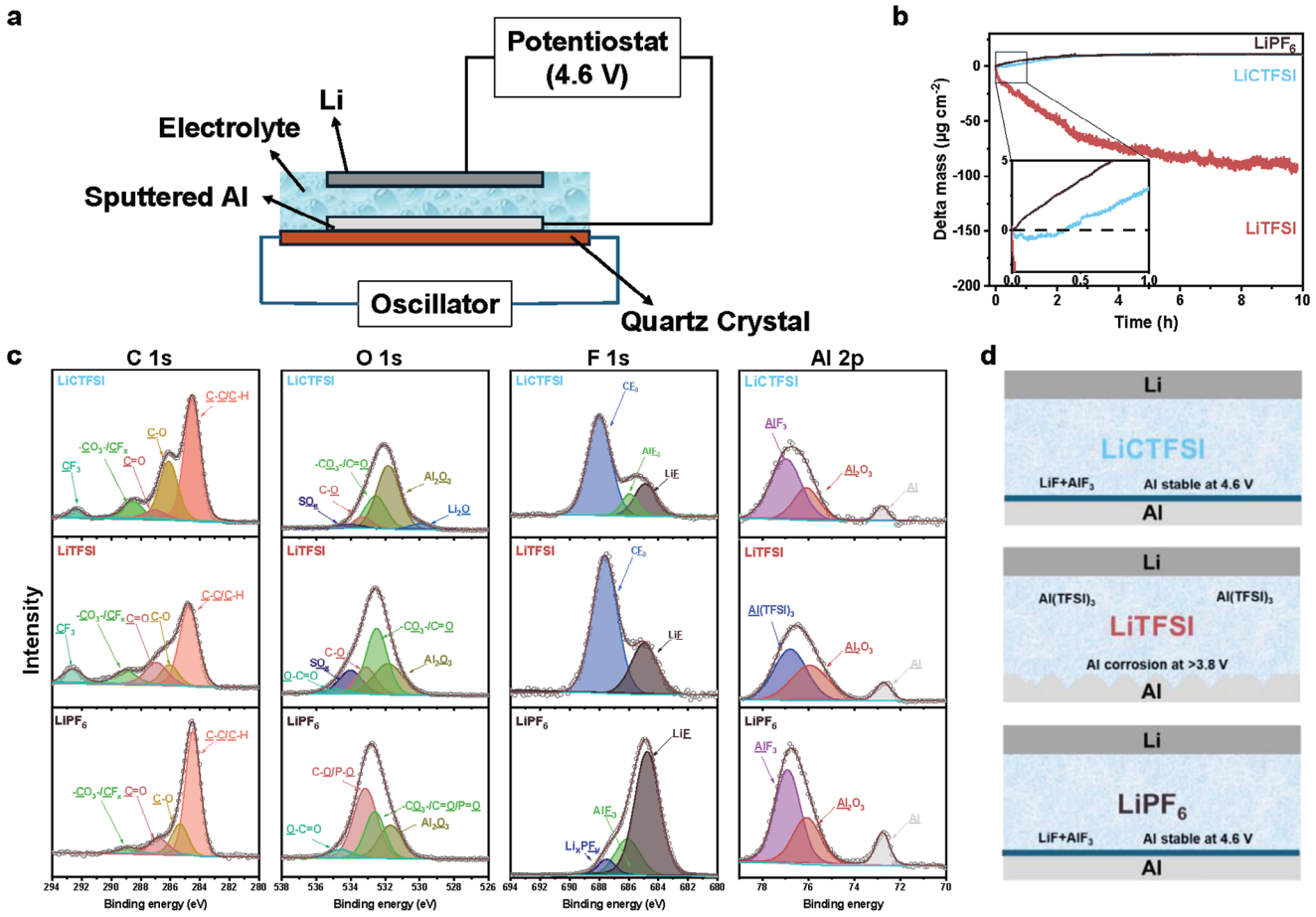

Figure 2. Analysis of the corrosion mechanisms of electrolytes with different lithium salts by electrochemical quartz crystal microbalance (eQCM) and XPS techniques. a) Schematic of the working mechanism of eQCM. b) Mass changes in the sputtered Al layer on the quartz crystal during potentiostatic tests of Li||Al cells using electrolytes of PC-FEC with 2 M LiCTFSI, LiTFSI, and $LiPF_6$. The inset image provides a detailed zoom-in of the first hour. c) XPS spectra of the Al electrodes after the potentiostatic tests in various electrolytes, including C 1s spectra, O 1s spectra, F 1s spectra, and Al 2p spectra. d) Schematic illustration of the electrochemical behavior of the Al electrode in LiCTFSI- and LiTFSI-based electrolytes.

remain smooth, showing minimal impact after the potentiostatic tests. In contrast, significant pitting corrosion on the Al was observed when using the LiTFSI electrolyte, indicating that the Al current collector anodically dissolved in the LiTFSI-based electrolyte at elevated potentials. Furthermore, the EDX mapping results at selected areas reveal that F is uniformly distributed on the surface of the Al electrode in both LiCTFSI and $LiPF_6$ electrolytes (Figure 1e), confirming the formation of a robust LiF and AlF_3 passivation layer. In sharp contrast, in the LiTFSI-based electrolyte, F is almost undetectable outside of the pitting holes because the dissolved $Al(TFSI)_3$ fails to decompose and form an effective passivation layer on the Al electrode.

Electrochemical quartz crystal microbalance (eQCM) was used to investigate the passivation mechanism of LiCTFSI on the Al current collector. eQCM technique, with its ability to detect mass changes to the accuracy of ng cm^{-2}, can effectively quantify SEI mass loss and dissolution in lithium metal batteries.[20,21] **Figure** 2a illustrates the methodology, where we applied a constant voltage of 4.6 V to ≈100 nm Al-coated quartz crystal. Lithium metal was used as the counter and reference electrode. The change in oscillation frequency of the quartz crystal is recorded during the potentiostatic tests, and the corresponding mass changes can be calculated based on Sauerbrey's equation (see Experiment Section). As depicted in Figure 2b, a rapid mass decrease is observed in LiTFSI electrolyte after applying the voltage, which indicates severe and continuous corrosion of the Al. In contrast, when using LiCTFSI and $LiPF_6$ electrolytes, the mass gradually increases and reaches a stable value of ≈ +10 μg cm^{-2} after ≈2 h, suggesting the formation of a passivation layer and effectiveness in protecting the Al current collector. It should be noted that the behavior of the LiCTFSI-based electrolyte in the initial period of ≈ 1 h differs markedly from that of the $LiPF_6$ electrolyte (inset image of Figure 2b). The mass in the LiCTFSI-based electrolyte slightly decreases initially, followed by an increase, while the mass in $LiPF_6$ electrolyte exhibits a direct increase in mass from the beginning. The mass changes in Figure 2b consist of the current change in Figure 1b.

We also performed X-ray photoelectron spectroscopy (XPS) analysis on the surface of the Al after the potentiostatic tests conducted in various electrolytes. The Al 2p spectra in Figure 2c reveals that all Al electrodes display peaks corresponding to metallic Al and the original Al_2O_3. Strong AlF_3 signal at 76.7 eV in Al

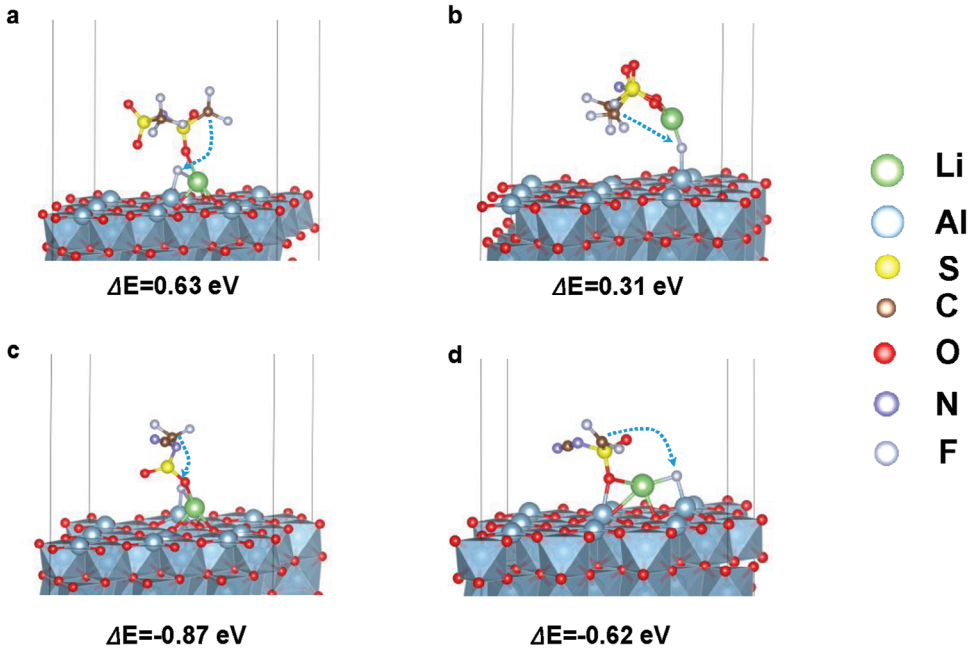

Figure 3. The defluorination reaction and the corresponding reaction energy of LiTFSI and LiCTFSI on α-Al_2O_3 surface. a,b) show two possible defluorination pathways of LiTFSI, c,d) show two possible defluorination pathways of LiCTFSI.

2p are detected in both LiCTFSI and $LiPF_6$ electrolytes, which is also confirmed in the F 1s spectrum. Strong LiF signals at 685 eV are detected from the Al surface after the potentiostatic tests. Consequently, the observed reduction in corrosion and enhanced performance can be attributed to the formation of a robust protective layer, rich in AlF_3 and LiF. In sharp contrast, in the LiTFSI-based electrolyte, neither AlF_3 nor LiF was detected. Instead, $Al(TFSI)_3$ is preferentially formed through the reaction with the $TFSI^-$ anion, which can be confirmed from the strong CF_3 signal in C 1s and F 1s spectra. In addition, the signals of Al_2O_3 is far weaker than the $Al(TFSI)_3$, indicating the attack of LiTFSI toward the oxidation layer on the Al surface. The dissolution of $Al(TFSI)_3$ into electrolytes due to the high solubility in carbonate solvents exposes fresh Al for the further attack from LiTFSI.[12] In $LiPF_6$-based electrolytes, the decomposition of $LiPF_6$—initiated by the trace amounts of moisture or the electrochemical oxidation of solvent molecules—can produce HF. The HF can then facilitate the creation of an AlF_3 layer, which physically passivates the aluminum current collector and protects it from corrosion.[22] Figure 2d demonstrates the different behavior of LiCTFSI, LiTFSI, and $LiPF_6$ electrolytes on Al current collector. In LiCTFSI-based electrolyte, the LiCTFSI first attacks the Al_2O_3 layer, leading to a small current density increase during the potentiostatic tests and the mass decrease detected in the eQCM test. However, the attack in the LiCTFSI electrolyte ceases quickly. The $CTFSI^-$ subsequently decomposes into a protective layer rich in LiF and AlF_3, which effectively prevents corrosion of Al.[16,23,24]

In order to further study the mechanism of the protective behavior of LiCTFSI on the Al current collector, which is covered by Al_2O_3, the defluorination reaction of LiTFSI and LiCTFSI on the surface of α-Al2O3 was investigated using density functional theory (DFT). The reactions were modeled as a two-step process (**Figure 3**, Figures S7 and S8, Supporting Information). First, the Li^+-$TFSI^-$ and Li^+-$CTFSI^-$ ion pairs were absorbed onto the (001) surface of α-Al_2O_3. Then, F was transferred from the anion to the α-Al_2O_3 surface. The possibility of the defluorination reaction was evaluated thermodynamically using reaction energy. DFT calculations show that the Li^+-$TFSI^-$ and Li^+-$CTFSI^-$ ion pairs can be adsorbed onto the α-Al_2O_3 surface in two possible configurations. In one configuration, Li directly coordinates with the O atoms of α-Al_2O_3 and the anion (Figures S7a and S8a, Supporting Information), while in the other configuration, the Li^+-anion pair is positioned parallel to the surface without direct coordination (Figures S7c and S8c, Supporting Information). Upon defluorination, the adsorption structure undergoes significant reorganization (Figures S7b,d and S8b,d, Supporting Information). Reaction energy calculations indicate that the defluorination reaction of LiCTFSI is spontaneous due to negative reaction energy ($E_{reaction}$ =−0.87 and−0.62 eV), whereas that of LiTFSI is thermodynamically unfavorable ($E_{reaction}$ = 0.63 and 0.31 eV). The defluorination reaction of LiCTFSI results in the formation of Al-F-Li compounds (Figure S8b,d, Supporting Information), which help prevent corrosion of the current collector.

4. Performance of NCM811 Cathodes

The performance of NCM811 cathode on Al current collector was evaluated in NCM811||Li half cells in a voltage range of 2.8–4.6 V with LiCTFSI and $LiPF_6$ electrolytes. The mass loading of NCM811 is ≈10 mg cm^{-2}, corresponding to an area loading of ≈2.1 mAh cm^{-2}. A Ti foil was placed between the cathode and the coin cell in case to avoid stainless-steel corrosion. NCM811 cathodes were initially charged/discharged at a low rate of 0.1C (where 1C = 210 mAh g^{-1}) to activate the cathodes, then the cycling rate was increased to 0.3C for 20

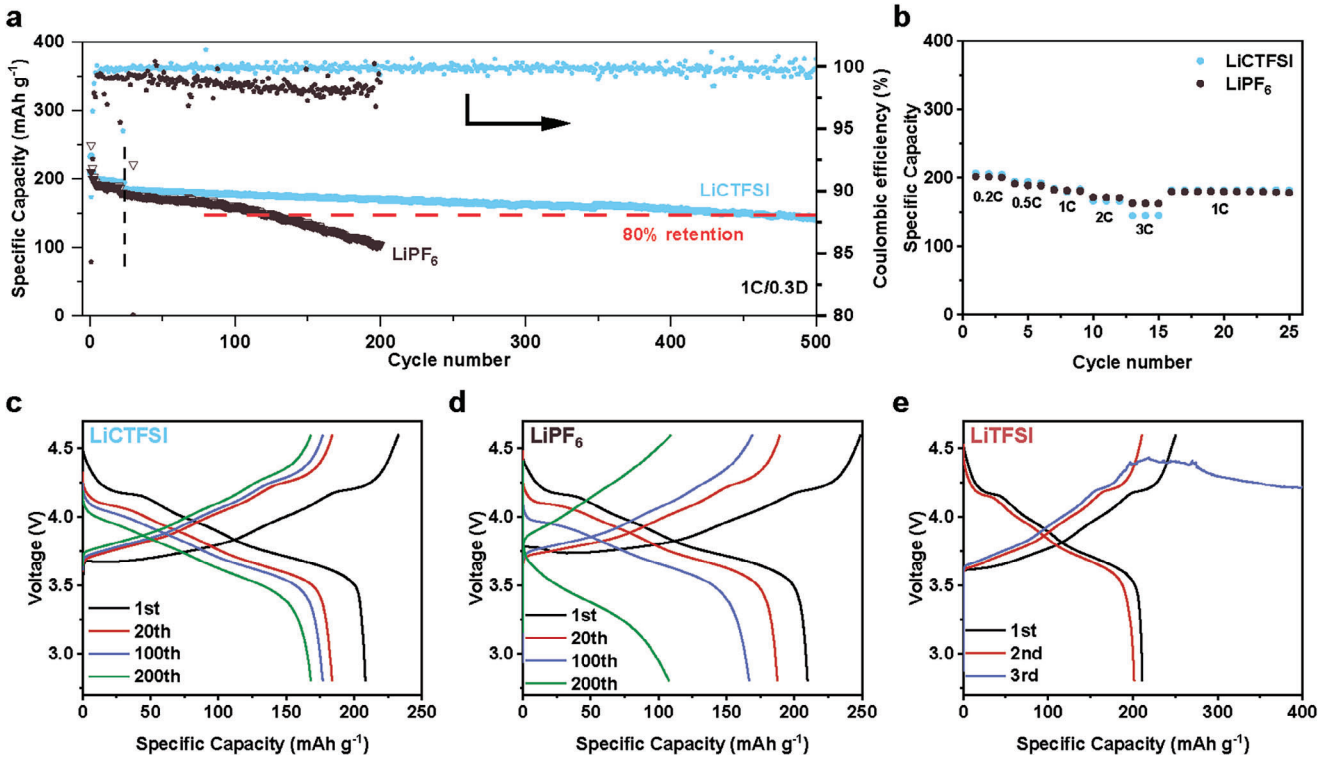

Figure 4. Electrochemical performance of NCM811||Li half cells. a) Cycling performance for cells with electrolytes of PC-FEC containing 2 M LiCTFSI and 2 M $LiPF_6$. b) Rate performance of cells using 2 M LiCTFSI and 2 M $LiPF_6$ PC-FEC electrolyte. c–e) Voltage profiles of cells employing electrolytes of PC-FEC with 2 M LiCTFSI, 2 M $LiPF_6$, and 2 M LiTFSI, respectively.

charge/discharge cycles. After that, the charge rate was further increased to 1C, while the discharge rate was still maintained at 0.3C (noted 1C/0.3D) for the rest of the cycles. In **Figure** 4a,c, the NCM811 cathodes with the 2 M LiCTFSI PC-FEC electrolyte maintain 80.3% capacity retention at 500 cycles, with an average CE of 99.89%. In contrast, capacity of NCM811 cathode with $LiPF_6$-based electrolytes dropped over 40% after 200 cycles, with an average CE of only 98.45% (Figure 4a,d). The high transference number (0.80) of the 2 M LiCTFSI PC-FEC electrolytes also enables NCM811 cathodes to achieve a high-rate performance (Figure 4b; Figure S9, Supporting Information). At room temperature, the half cells deliver capacities of 205.1, 194.3, 183.6, 166, and 145 mAh g^{-1} at rates of 0.2C, 0.5C, 1C, 2C and 3C, respectively. NCM811 cathodes in LiTFSI electrolytes can only charge/discharge for three cycles (Figure 4e). At the third cycle, severe and continuous corrosion prevents the cell from charging to the predetermined voltage. Severe corrosion is also observed in the LiFSI-based electrolyte, and the NCM811 half-cells cannot even be charged above 4.4 V in the LiFSI PC-FEC electrolyte (Figure S10, Supporting Information). Moreover, the half-cells with LiCTFSI-based electrolyte exhibit much better high-temperature performance than those with $LiPF_6$-based electrolyte, as depicted in Figure S11 (Supporting Information). Given the thermal instability of $LiPF_6$, the cells with $LiPF_6$-based electrolyte suffered significant capacity decay after 100 cycles at 60 °C, maintaining only 42% capacity. In contrast, the NCM811 cathodes with LiCTFSI-based electrolyte can maintain 87.9% capacity with an average CE of 99.2% due to the high thermal stability of LiCTFSI electrolytes at 60 °C.

To gain a more comprehensive understanding of the NCM811 cathode in LiCTFSI electrolytes, we proceeded with a series of post-mortem analyses on the cycled NCM811 cathode. The High-Resolution Transmission Electron Microscopy (HR-TEM) images of the NCM811 cathode after 200 cycles in LiCTFSI and $LiPF_6$ electrolytes are presented in **Figure** 5a,b. The CEI on the NCM811 cathode in LiCTFSI electrolyte is thinner (≈2 nm), more compact, and more homogeneous than that in the $LiPF_6$ electrolyte (≈15 nm). The thick CEI in the $LiPF_6$-based electrolyte leads to poorer kinetic performance. This effect is evidenced by significantly higher overpotentials, as illustrated in Figure 4c,d, which can also be seen in the Electrochemical Impedance Spectroscopy (EIS) results presented in Figure S12 (Supporting Information). In addition, the presence of granular LiF CEI (Figure 5b) on the NCM811 in $LiPF_6$-based electrolyte, comes from the serious corrosions by HF in the $LiPF_6$-based electrolyte, which further verified the severe sensitivity of $LiPF_6$ to the moisture.[25] To further understand the interfacial chemistry, the interphase layers of the cycled NCM811 cathodes were characterized by XPS, as shown in Figure 5c,d, and Figure S13 (Supporting Information). A strong LiF signal located at 685.0 eV of the cycled NCM811 in LiCTFSI electrolyte as shown in the F 1s spectra only appears on the top surface. After 240 seconds of etching, almost no LiF signal is detected. The C 1s spectra signals show a decrease in C-F bonds, suggesting that LiCTFSI decomposes to form a thin but protective, LiF-rich layer on the cathode surface, without causing

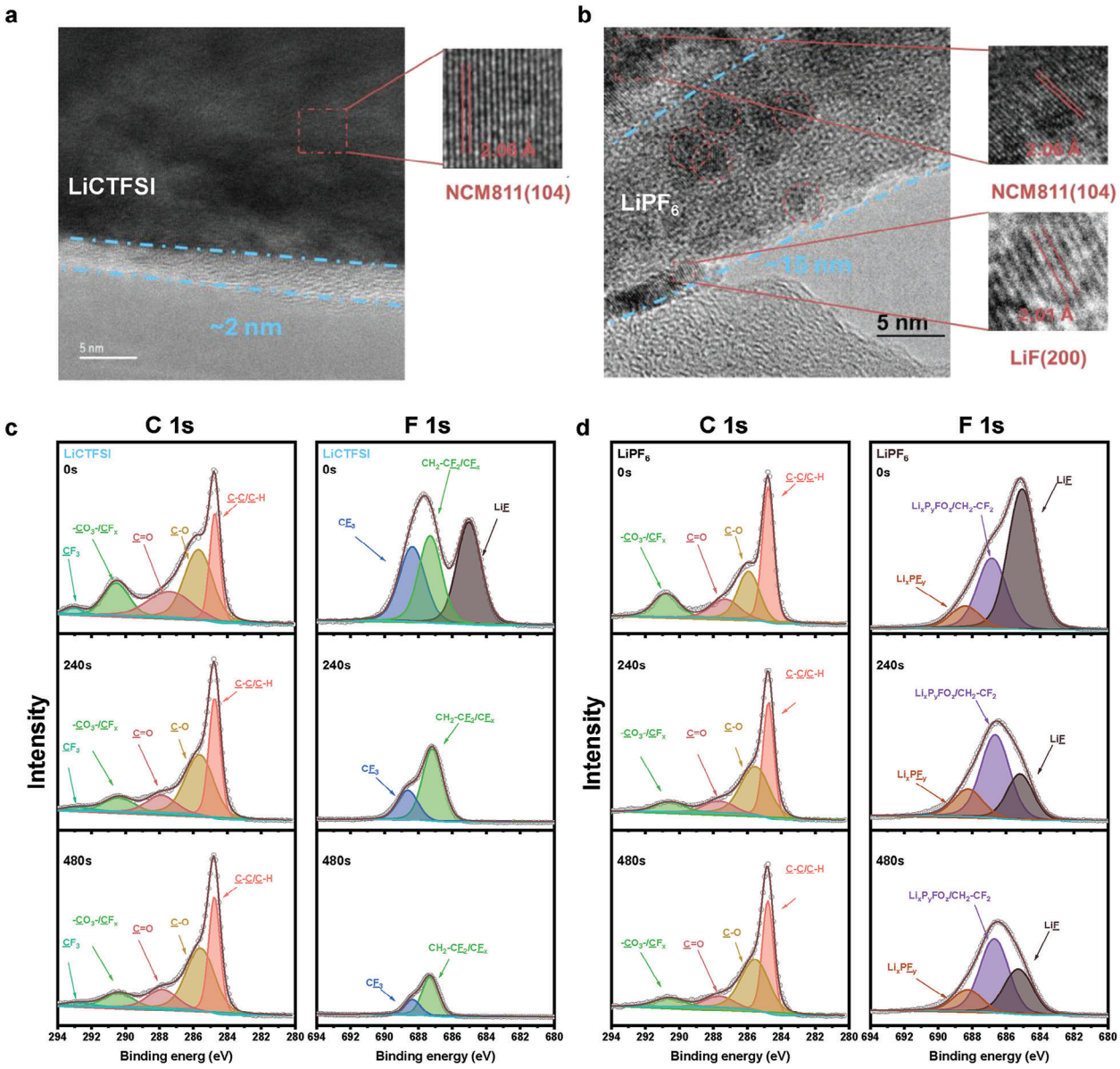

Figure 5. Post-mortem analyses of the NCM811 cathode in various electrolytes of PC-FEC with 2 M LiCTFSI and $LiPF_6$. a, b) HR-TEM images and lattice fringes patterns of cathode after 200 cycles, highlighting selected areas. c, d) XPS spectra of cathode after 200 cycles, including C 1s and F 1s spectra.

corrosion deeper inside the cathode. Contrastingly, in the $LiPF_6$ electrolyte, strong LiF signals are detected in the CEI of NCM811 cathode. The presence of signals at 686.5 eV (F 1s) for $Li_xP_yFO_2$ and at 688.2 eV (F 1s) for Li_xPF_y further confirms the decomposition of $LiPF_6$. Combining with the TEM result, it's evident that the thick layer filled with granular LiF in the $LiPF_6$ electrolyte cannot protect the cathode from corrosion as effectively as the thinner, more compact CEI layer found with the LiCTFSI electrolyte. Furthermore, the pristine and the cycled NCM811 cathodes using these two liquid electrolytes were well characterized by X-ray diffraction (XRD), and the corresponding XRD patterns are shown in Figure S14 (Supporting Information). The diffraction peaks of cycled NCM811 cathodes are slightly shifted to a lower 2θ degree, demonstrating the expansion of crystal lattice due to volume changes of the NCM unit cells during Li^+ ions intercalation and deintercalation processes.[26,27] Additionally, the integrated intensity ratio of I(003)/I(104) decreases from the original 1.51 to 1.42 (LiCTFSI) and 1.33 ($LiPF_6$) after 200 cycles, respectively, indicating more cation mixing of NCM811 in the $LiPF_6$ electrolyte after cycling.[28,29]

5. NCM811/Graphite Full-Cell Performance

To assess the practical suitability of the LiCTFSI-based electrolyte in Li-ion batteries, we paired the NCM811 cathode with a graphite (Gr) anode. The capacity ratio between the negative and positive electrodes (N/P ratio) is maintained within the range of 1.05–1.10. We first evaluated the performance of graphite an-

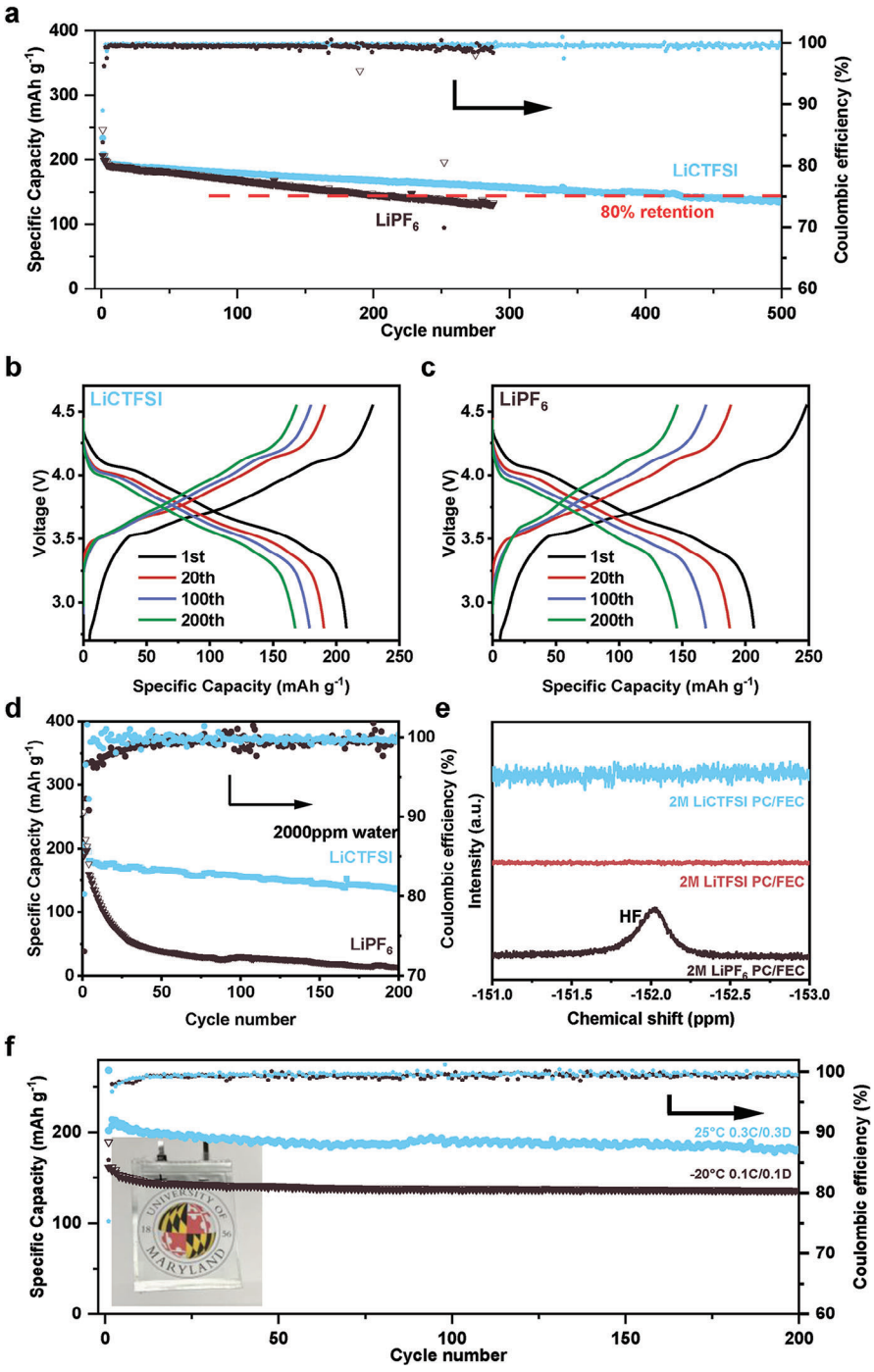

Figure 6. Electrochemical performance of NCM811||Gr full Cells and moisture tolerance evaluation. a) Cycling performance of cells containing 2 M LiCTFSI and 2 M $LiPF_6$ in PC-FEC electrolytes. Voltage profiles of the full cells at 1st, 20th, 100th, and 200th cycles with electrolytes of b) 2 M LiCTFSI PC-FEC and c) 2 M $LiPF_6$ PC-FEC. d) Cycling performance of cells with 2 M LiCTFSI PC-FEC and 2 M $LiPF_6$ PC-FEC electrolytes containing 2000 ppm water. e) ^{19}F NMR patterns for electrolytes of 2 M LiCTFSI, LiTFSI, $LiPF_6$ in PC-FEC (with 2000 ppm water). f) Cycling performance of pouch cells with 2 M LiCTFSI PC-FEC electrolyte at room temperature and −20 °C.

ode in LiCTFSI electrolyte. As shown in Figure S15a (Supporting Information), the graphite anodes in LiCTFSI electrolyte exhibit long cycle stability, and a higher N 1s signal in the XPS was detected on the graphite anode cycled in LiCTFSI electrolyte (Figure S15b, Supporting Information). The L_3N-rich SEI on the graphite has been proven to be beneficial for low-temperature and fast-charge performance.[30] **Figure 6a** shows the cycling performance of NCM811||Gr full cells in LiCTFSI and $LiPF_6$ electrolytes at room temperature. Because of the 5%-10% excess Gr anode, the cut-off voltage of the full cell was adjusted

to 2.8–4.55 V. The cells were cycled at a 1C charge and 0.3C discharge rate after two initial activation cycles at 0.1C. The cells utilizing the LiCTFSI electrolyte demonstrated a capacity retention of 77.8% after 500 cycles, whereas the cells with the $LiPF_6$ electrolyte experienced a decline to 80% capacity after just 200 cycles (Figure 6a). The NCM811||Gr full cells with commercial electrolyte (1M $LiPF_6$ EC-DEC) also drop to 70% capacity after only 100 cycles (Figure S16, Supporting Information). The charge/discharge overpotentials in the $LiPF_6$ electrolyte is much larger than that in LiCTFSI electrolyte, as illustrated in Figure 6b,c. As illustrated in XPS in Figure S17 (Supporting Information), the Ni signal on the surface of recovered graphite anodes is significantly higher when using the $LiPF_6$ electrolyte compared to the LiCTFSI-based electrolyte. This observation confirms the corrosive effect of HF on the cathode and the migration of transition metals in $LiPF_6$ electrolyte. Moreover, at a high temperature of 60 °C (Figure S18, Supporting Information), the full cells employing a LiCTFSI-based electrolyte exhibit 94.2% capacity retention after 100 cycles, with an average CE of 99.45%, whereas cells with a $LiPF_6$-based electrolyte can only maintain 52.7%.

6. Moisture Tolerance and Low-Temperature Performance of NCM811/Gr Full Cells

Besides their excellent performance under normal conditions, the LiCTFSI electrolytes also enable NCM811||Gr full cells to have exceptional tolerance to moisture. We mix the PC-FEC solvent with 2000 ppm water, and then add the $LiPF_6$ or LiCTFSI salts into water-contained PC-FEC solvents. The $LiPF_6$ electrolyte changed into a brown color after 24 h (see Figure S19, Supporting Information), indicating its severe decomposition. In contrast, the LiCTFSI electrolytes still maintain transparency. The performance of NCM||Gr full cells employing the moisture-containing LiCTFSI- and $LiPF_6$- electrolyte are shown in Figure 6d. The cells employing the LiCTFSI-based electrolyte exhibited only a ≈3% decrease in the initial CE, as shown in Figure S20 (Supporting Information), and maintained normal cycling performance in subsequent cycles. In contrast, NCM||Gr full cells using the moisture-contained $LiPF_6$-based electrolyte demonstrated a faster capacity decay than in moisture-free environments, indicating that severe decomposition of $LiPF_6$ led to accelerated battery degradation. The results of the ^{19}F Nuclear Magnetic Resonance (NMR) analysis for the solvents and electrolytes are displayed in Figure 6e. As expected, a high concentration of HF was found in the $LiPF_6$-based electrolyte, correlating with the significant corrosion observed in the cathode in previous TEM images. Conversely, HF was not detected in either the pure solvent or in electrolytes formulated with LiCTFSI. Other than directly adding water inside the electrolytes, we also exposed the electrolytes to air (25 °C, 70% humidity) for 1 h and assembled the cells outside the glovebox. Figure S21 (Supporting Information) shows these cells had an initial CE of 71% and maintained 110 mAh g^{-1} after 200 cycles.

Owing to the design of the ethylene carbonate (EC)-free solvent, the PC-FEC-based electrolytes exhibit a low freezing point. In comparison to the electrolyte based on ethylene carbonate and dimethyl carbonate (EC/DEC) with a high freezing point of ≈−20 °C, the 2 M LiCTFSI PC-FEC electrolyte showed no phase change over the temperature range of −90 °C to +25 °C, as illustrated differential scanning calorimetry (DSC) (Figure S22, Supporting Information). Attributable to the low freezing point and the reduced desolvation energy of Li^+ ions in FEC,[31–33] the full cells employing LiCTFSI-based electrolyte demonstrate good performance at low temperatures. Figure S23a (Supporting Information) illustrates that, at a 0.1C charge/discharge rate, the full cells maintain capacities of 210.6, 196.8, 168.4, and 123.4 mAh g^{-1} at temperatures of 25, 0,−20, and −30 °C, respectively. As a reference, the same cells with commercial electrolyte (1M $LiPF_6$ EC-DEC, Figure S23b, Supporting Information) can only achieve 210.2, 140.5, and 71.2 mAh g^{-1} at temperatures of 25, 0, and −20 °C, respectively. For more practical cases and potential scale-up conditions, we assembled single-layer NCM811||Gr pouch cells employing LiCTFSI-based electrolytes. The cycle performance at room temperature and −20 °C are shown in Figure 6f. The pouch cells exhibit a capacity of 205 mAh g^{-1} (0.3C/0.3D) and maintain 88.9% of this capacity after 200 cycles at room temperature. Meanwhile, when operated at −20 °C, the pouch cells display a capacity of 155 mAh g^{-1} (0.1C/0.1D) and maintain 92.1% after 200 cycles, demonstrating their potential scalability for high-voltage lithium-ion batteries.

7. Conclusion

We developed LiCTFSI/PC-FEC electrolytes that have a wide electrochemical stability window (0.0-4.6V), wide operation temperature window (−20 °C to +60 °C), high passivation to Al current collector, high moisture tolerant capable of assembly NCM811/graphite full cell in the air. The electrolyte passivation to Al current collector comes from the electrolyte's ability to form a protective layer rich in LiF and AlF_3 derived from $CTFSI^-$ decomposition, which effectively prevents the Al pitting corrosion often seen in LiTFSI-based electrolytes. A significant outcome of using LiCTFSI is a marked decrease in hydrofluoric acid (HF) generation, leading to enhanced battery life and efficiency. As demonstrated in the NCM811 half-cells utilizing a 2 M LiCTFSI PC-FEC electrolyte at a 4.6 V cut-off, a capacity retention of 80.3% after 500 cycles is achieved, alongside an average CE of 99.89%. Full cells paired with a graphite anode similarly showed 77.8% capacity retention over 500 cycles. The electrolyte's low freezing point and high thermal stability enable the full cell to operate across a wide temperature range of −20 to 60 °C. Remarkably, the electrolyte's resistance against moisture—capable of handling up to 2000 ppm water—has the potential to significantly streamline battery manufacturing processes and reduce costs, given the less stringent environmental control requirements. This research encourages further exploration into innovative electrolytes with distinct physical and chemical traits, offering a promising direction for future high-energy, cost-effective lithium-ion batteries.

8. Experimental Section

Materials and Electrolytes: Propylene carbonate (PC) was purchased from Sigma and used after being dehydrated with a 4-Å molecular sieve. Fluoroethylene carbonate (FEC), Lithium bis(trifluoromethane)sulfonimide (LiTFSI), Lithium Hexafluorophosphate ($LiPF_6$), purchased from Gotion, were used as received. LiCTFSI, purchased from PROVISCO CS, was used as received. The water content

of the solvents, determined using a Karl Fischer aquameter, was measured to be 5 ppm or less. The 2 M LiCTFSI-, LiTFSI-, $LiPF_6$-based electrolytes were prepared by dissolving the corresponding salts in PC-FEC (7:3 by volume) inside a glove box (O_2<0.1 ppm, H_2O<0.1 ppm). Water-containing electrolytes were made by blending the corresponding electrolytes with a specific amount of water. Electrolytes are usually kept in plastic bottles but moved to clear glass bottles for photos.

Electrodes: $LiNi_{0.8}Mn_{0.1}Co_{0.1}O_2$ (NCM811) cathode coatings on aluminum foil were kindly supplied by Saft America. These electrodes consist of 94 wt.% NCM811, 3 wt.% carbon, and 3 wt.% polyvinylidene fluoride (PVDF), featuring ≈30% porosity and an area capacity of 2.1 mAh cm^{-2} (with a mass loading of ≈ 10 mg cm^{-2}). Graphite powders were sourced from MSE Supplies. Graphite electrodes were prepared by blending graphite, carbon black, and PVDF in a volume ratio of 90:4:6, using N-methyl pyrrolidinone (NMP) as the solvent. The slurry was cast onto copper foil, then dried at 80 °C overnight under vacuum. The graphite electrodes have an area capacity of ≈2.3 mAh cm^{-2}, yielding an N/P ratio of 1.05–1.1. These electrodes were cut into 0.63 cm^2 sheets and subjected to vacuum drying at 80 °C for 24 h prior to assembly.

Electrochemical Measurements: CR2032 coin cells were assembled by placing a Celgard 3501 separator between the graphite/lithium anodes and the NCM811 cathodes or Al current collector. A fixed volume (30 µl) of liquid electrolyte was used in each cell. The contant-current/constant-voltage tests were conducted in Landt battery tester. The potentiostatic corrosion tests on Li||Al cells were carried out by applying a CV charge of 4.6 V. The NCM811||Li cells were initially formed at a rate of 0.1C, cycling between 2.8 and 4.6 V. After completing 20 cycles at a 0.3C charge/discharge rate, the cells were then cycled at a 1C charge and 0.3C discharge rate for the subsequent cycles, with the C-rate defined as 1C = 210 mAh g^{-1}. The NCM811||Gr cells underwent an initial formation at a rate of 0.1C, with cycling occurring between 2.8 and 4.55 V. Following this initial phase, the cells were cycled at a rate of 1C for charging and 0.3C for discharging in the subsequent cycles. For pouch cells, Al and Ni strips were attached as electrode tabs to the cathode and anode sides, respectively. The components used—electrodes, separators, and liquid electrolytes—were identical to those in the coin cells. Single-layer pouch cells (5 cm × 7 cm) were vacuum-sealed in glove box with a fixed electrolyte of 3.0 g Ah^{-1}. Impedance spectra for the cells were measured using a Gamry electrochemical workstation, employing a frequency range from 0.01 to 1000000 Hz. The transference number t+ was calculated by the following Equation (1):

$$t_+ = \frac{I_s\,(\Delta V - I_0 R_0)}{I_0\,(\Delta V - I_S R_S)} \tag{1}$$

where ΔV is the voltage polarization applied, I_s and R_s are the steady-state current and resistance, I_0 and R_0 are the initial current and resistance, respectively. The applied voltage bias for the tests in the Li||Li cells here was 10 mV.

Characterization: All the samples recovered from the cycled cells were washed with PC solvent to remove any residual Li salts from the surface of the electrodes and vacuum-dried before the characterizations. SEM (Hitachi SU-70 field emission scanning electron microscope) and TEM (JEOL-JEM 2100F) are equipped with energy-dispersive spectroscopy (EDS, Bruker X-Flash 6/60 series). XPS experiments were conducted using a high-resolution Kratos AXIS 165 spectrometer, employing monochromatic Al Kα radiation. To prevent any exposure to air and moisture, samples were transported directly from the glovebox to the XPS instrument. The neutralizer was applied during the data collection, and an Ar sputter gun was used for the etching with the ion energy set at 200 eV and the middle range current selected. The etching procedure was carried out in a cycle of accumulated 0, 240, and 480 s. All data was calibrated based on the C 1s peak to 284.8 eV for binding energy values. The ^{19}F-NMR spectra were recorded on a Varian Mercury 400 MHz NMR spectrometer at room temperature. X-ray powder diffraction (XRD) was performed on D8 Advance with LynxEye and SolX (Bruker) using Cu Kα radiation. Attenuated total reflectance Fourier transform infrared (ATR-FTIR) spectra were recorded via Bruker instrument in 3500–600 cm^{-1}range with accumulating 10 scans per spectra by directly dripping samples on a diamond single crystal. eQCM measurements were performed using an eQCM 10 M Quartz Crystal Microbalance from Gamry Instruments, Inc. A 100-nm Al layer was sputtered onto the quartz crystal using the AJA ATC 1800 Sputtering unit. This Al-coated quartz crystal served as the working electrode. For the counter and reference electrode, we used Li metal. The nominal electroactive area was 1.1 cm^2, while the nominal area of overlap was 0.24 cm^2. The eQCM cell was assembled in a glovebox filled with argon, maintaining an O_2/H_2O concentration of <0.1 ppm. We connected the eQCM to a Landt battery test system for electrochemical tests conducted at 25 °C. The mass change was calculated using the Sauerbrey Equation (2):

$$\Delta f = -\frac{2 f_0^{\,2}}{A\sqrt{\mu_q \rho_q}}\Delta m \tag{2}$$

Here, f_0 represents the fundamental frequency of the crystal, A is the piezoelectrically active crystal area, and μ_q and ρ_q are the shear modulus and density of the quartz, respectively. The mass change (Δm) can be determined based on the frequency change (Δf).

Calculations: The Vienna Ab initio Simulation Package (VASP 6.3)[34] was used to perform DFT calculations. The Perdew–Burke–Ernzerhof (PBE) realization[35] of the generalized gradient approximation (GGA) for the exchange-correlation[36] was adopted. The crystal structure of α-Al_2O_3 [R-3cH] was obtained from the Inorganic Crystal Structures Database (ID: 9770) and reoptimized with an energy cutoff of 520 eV. Al_2O_3 surface slabs were generated from 3 × 3 × 1 size supercells by cutting along the (001) direction.[37] A vacuum of 25 Å was added along the perpendicular axis. The Li^+-anion pair was optimized independently and then placed in the vacuum region above the α-Al_2O_3 surface. Five initial adsorption configurations were generated with different Li^+-anion pair projection directions and distances relative to the Al_2O_3 surface. The initial configurations were optimized and converged to 10^{-4} eV in energy and 10^{-3} eV $Å^{-1}$ in forces. A dipole correction was applied along the perpendicular axis in the surface calculations. F was then manually moved from the anion to the Al_2O_3 surface in the optimized structure, and the structure was reoptimized. The reaction energy was calculated by subtracting the energy of the adsorbed state from that of the defluorinated state:

$$E_{reaction} = E_{defluorinated} - E_{adsorbed} \tag{3}$$

where $E_{adsorbed}$ and $E_{defluorinated}$ are the total energy of the system in an adsorbed state and defluorinated state.

Supporting Information

Supporting Information is available from the Wiley Online Library or from the author.

Acknowledgements

This work was supported by the U.S. Department of Energy, Basic Energy Science, (Award No. DE-SC0023408 (X.J., D.J., and C.W.).

Conflict of Interest

The authors declare no conflict of interest.

Data Availability Statement

The data that support the findings of this study are available from the corresponding author upon reasonable request.

Keywords

extreme electrolyte, high-voltage cathode, lithium-ion battery, moisture-tolerance, novel salt

Received: June 5, 2024
Revised: October 9, 2024
Published online:

[1] J. M. Tarascon, M. Armand, *Nature* **2001**, *414*, 359.
[2] B. Dunn, H. Kamath, J. M. Tarascon, *Science* **2011**, *334*, 928.
[3] X. Fan, C. Wang, *Chem. Soc. Rev.* **2021**, *50*, 10486.
[4] W. Li, E. M. Erickson, A. Manthiram, *Nat. Energy* **2020**, *5*, 26.
[5] L. Su, K. Jarvis, H. Charalambous, A. Dolocan, A. Manthiram, *Adv. Funct. Mater.* **2023**, *33*, 2213675.
[6] B. L. D. Rinkel, J. P. Vivek, N. Garcia-Araez, C. P. Grey, *Science* **2022**, *15*, 3416.
[7] M. Liu, J. Vatamanu, X. Chen, L. Xing, K. Xu, W. Li, *ACS Energy Lett.* **2021**, *6*, 2096.
[8] M. Dahbi, F. Ghamouss, F. Tran-Van, D. Lemordant, M. Anouti, *J. Power Sources* **2011**, *196*, 9743.
[9] N. P. Pieczonka, Z. Liu, P. Lu, K. L. Olson, J. Moote, B. R. Powell, J.-H. Kim, *J. Phys. Chem. C* **2013**, *117*, 15947.
[10] J. Xiang, Y. Wei, Y. Zhong, Y. Yang, H. Cheng, L. Yuan, H. Xu, Y. Huang, *Adv. Mater.* **2022**, *34*, 2200912.
[11] C. Wang, L. Ouyang, W. Fan, J. Liu, L. Yang, L. Yu, M. Zhu, *J. Alloys Compd.* **2019**, *805*, 757.
[12] C. Wang, L. Yu, W. Fan, J. Liu, L. Ouyang, L. Yang, M. Zhu, *ACS Appl. Mater. Interfaces* **2017**, *9*, 9630.
[13] S. Wang, W. Qiu, Y. Guan, B. Yu, H. Zhao, W. Liu, *Electrochim. Acta* **2007**, *52*, 4907.
[14] L. Qiao, U. Oteo, M. Martinez-Ibanez, A. Santiago, R. Cid, E. Sanchez-Diez, E. Lobato, L. Meabe, M. Armand, H. Zhang, *Nat. Mater.* **2022**, *21*, 455.
[15] T. M. Tekaligne, H. K. Bezabh, S. K. Merso, K. N. Shitaw, M. A. Weret, Y. Nikodimos, S. K. Jiang, S. C. Yang, C. H. Wang, S. H. Wu, W. N. Su, B. J. Hwang, *J. Mater. Chem. A* **2024**, *12*, 2157.
[16] K. Matsumoto, K. Inoue, K. Nakahara, R. Yuge, T. Noguchi, K. Utsugi, *J. Power Sources* **2013**, *231*, 234.
[17] C. Han, G. Chen, Y. Ma, J. Ma, X. Shui, S. Dong, G. Xu, X. Zhou, Z. Cui, L. Qiao, G. Cui, *Energy Mater.* **2023**, *3*, 300052.
[18] F. Kita, H. Sakata, S. Sinomoto, A. Kawakami, H. Kamizori, T. Sonoda, H. Nagashima, J. Nie, N. V. Pavlenko, Y. L. Yagupolskii, *J. Power Sources* **2000**, *90*, 27.
[19] J. Xu, V. Koverga, A. Phan, A. M. Li, N. Zhang, M. Baek, C. Jayawardana, B. L. Lucht, A. T. Ngo, C. Wang, *Adv. Mater.* **2024**, *36*, 2306462.
[20] P. Sayavong, W. Zhang, S. T. Oyakhire, D. T. Boyle, Y. Chen, S. C. Kim, R. A. Vila, S. E. Holmes, M. S. Kim, S. F. Bent, Z. Bao, Y. Cui, *J. Am. Chem. Soc.* **2023**, *145*, 12342.
[21] B. Kwon, J. Lee, H. Kim, D.-M. Kim, K. Park, S. Jo, K. T. Lee, *J. Mater. Chem. A* **2021**, *9*, 24993.
[22] Q. Zheng, Y. Yamada, R. Shang, S. Ko, Y.-Y. Lee, K. Kim, E. Nakamura, A. Yamada, *Nat. Energy* **2020**, *5*, 291.
[23] A. Hofmann, M. Schulz, V. Winkler, T. Hanemann, *J. Electrochem. Soc.* **2014**, *161*, A431.
[24] S.-T. Myung, Y. Hitoshi, Y.-K. Sun, *J. Mater. Chem.* **2011**, *21*, 9891.
[25] W. Li, A. Dolocan, J. Li, Q. Xie, A. Manthiram, *Adv. Energy Mater.* **2019**, *9*, 1901152.
[26] X. Yu, Y. Wang, H. Cai, C. Shang, Y. Liu, Q. Wang, *Ionics* **2019**, *25*, 1447.
[27] I. Buchberger, S. Seidlmayer, A. Pokharel, M. Piana, J. Hattendorff, P. Kudejova, R. Gilles, H. A. Gasteiger, *J. Electrochem. Soc.* **2015**, *162*, A2737.
[28] S.-J. Sim, S.-H. Lee, B.-S. Jin, H.-S. Kim, *Sci. Rep.* **2020**, *10*, 11114.
[29] T. Ohzuku, A. Ueda, M. Nagayama, *J. Electrochem. Soc.* **1993**, *140*, 1862.
[30] D. Lu, R. Li, M. M. Rahman, P. Yu, L. Lv, S. Yang, Y. Huang, C. Sun, S. Zhang, H. Zhang, J. Zhang, X. Xiao, T. Deng, L. Fan, L. Chen, J. Wang, E. Hu, C. Wang, X. Fan, *Nature* **2024**, *627*, 101.
[31] N. Zhang, T. Deng, S. Zhang, C. Wang, L. Chen, C. Wang, X. Fan, *Adv. Mater.* **2022**, *34*, 2107899.
[32] C. Sun, X. Ji, S. Weng, R. Li, X. Huang, C. Zhu, X. Xiao, T. Deng, L. Fan, L. Chen, X. Wang, C. Wang, *Adv. Mater.* **2022**, *34*, 2206020.
[33] R. Wang, S. Zhang, S. Peng, Y. Tong, X. Hu, *Carb. Neutral.* **2024**, *3*, 6.
[34] G. Kresse, J. Furthmüller, *Phys. Rev. B* **1996**, *54*, 11169.
[35] W. Kohn, L. J. Sham, *Phys. Rev.* **1965**, *140*, A1133.
[36] J. P. Perdew, K. Burke, M. Ernzerhof, *Phys. Rev. Lett.* **1996**, *77*, 3865.
[37] J. Ahn, J. W. Rabalais, *Surf. Sci.* **1997**, *388*, 121.